Journal of Materials Chemistry A

RSC Publishing

PAPER

View Article Online
View Journal | View Issue

Electric double layer capacitor and its improved specific capacitance using redox additive electrolyte†

Cite this: *J. Mater. Chem. A*, 2013, **1**, 1086

S. T. Senthilkumar,[a] R. Kalai Selvan,*[a] Y. S. Lee[b] and J. S. Melo[c]

Halogen (iodide, I^-) added aqueous electrolyte facilitates the capacitive behaviour of biomass derived activated carbon based electric double layer capacitors. To produce economically viable electrodes in large scale for supercapacitors (SCs), the activated carbons (ACs) prepared from *Eichhornia crassipes* (common water hyacinth) by $ZnCl_2$ activation. The prepared ACs were characterized by XRD, Raman, FT-IR and surface area, pore size and pore volume analysis. The electrochemical properties of the SCs were studied using cyclic voltammetry (CV), galvanostatic charge–discharge (GCD), electrochemical impedance spectroscopy (EIS) and cycling stability. The $3I^-/I_3^-$, $2I^-/I_2$, $2I_3^-/3I_2$ and I_2/IO_3^- pairs produce redox peaks in CV and a large Faradaic plateau in charge–discharge curves. Similarly, I^- ions improves the good ionic conductivity (lower charge transfer resistance) at the electrode/electrolyte interface which was identified through EIS studies. The calculated specific capacitance and energy density was 472 F g^{-1} and 9.5 W h kg^{-1} in aqueous solution of 1 M H_2SO_4. Interestingly, nearly two-fold improved specific capacitance and energy density of 912 F g^{-1} and 19.04 W h kg^{-1} were achieved when 0.08 M KI was added in 1 M H_2SO_4 electrolyte with excellent cycle stability over 4000 cycles. Subsequently, this improved specific capacitance and energy density was compared with 0.08 M KBr added to 1 M H_2SO_4 (572 F g^{-1}, 11.6 W h kg^{-1}) and 0.08 M KI added to 1 M Na_2SO_4 (604 F g^{-1}, 12.3 W h kg^{-1}) as electrolytes.

Received 6th September 2012
Accepted 23rd October 2012

DOI: 10.1039/c2ta00210h

www.rsc.org/MaterialsA

1 Introduction

Electric double layer capacitors (EDLCs) are known as super-capacitors (SCs) and have received much interest in recent times worldwide owing to their potential applications in portable devices, electric vehicles and industrial equipment.[1,2] Besides, SCs function between classical capacitors and batteries in terms of their power density (>batteries) and energy density (>classical capacitors), further they possess some distinct advantages such as light weight, high safety, quick charging and superior durability relative to batteries.[3,4] It is well known that electrode active materials play a vital role in terms of their electrochemical performances. Metal oxides/hydroxides and polymers (redox materials) are used as electrodes in redox or pseudo-capacitors, where the redox reactions are responsible for their high capacitance.[5] Unfortunately, their cost and poor electrochemical stability are a drawback towards commercialization. On the other hand, in electric double layer capacitors (EDLCs), carbon (activated carbon, carbon nanotube and carbon aerogel) based materials are used that accomplish longer cycle life because they can store the charges by electrical attraction of electrolytic charges or ions as an electrical double layer (EDL) without any redox reactions and structural changes.[5] However, they have delivered lower specific capacitance than the redox based materials.[6a] In order to further enhance the capacitance of EDLCs, different methods have been adopted such as preparing composites with redox materials[6b,c] and introduction of heteroatoms such as oxygen,[7,8] nitrogen,[8,9] phosphorus[10] and boron[11] in the carbon skeleton.

Among the carbon based materials, activated carbons (ACs) have been widely studied which offer numerous and miscellaneous applications for supercapacitors, batteries, hydrogen storage, electrochemical catalysis, sensors, and for water and air purification, and so on,[12,13] due to their significant properties such as high surface area, micro-to-nano porosity, easy processibility, high abundance, low cost, resistance to corrosion and high endurance at high temperatures.[14] Hence, in the last decade there has been much research on activated carbons for supercapacitor applications, and notably biomass derived activated carbons. Biomass is considered as an ideal precursor for the large scale production of activated carbon because of high availability and accessibility. Biomass is rich in carbon and oxygen atoms so one can produce the activated carbons in the presence of oxygen by a single step. It is well known that the physical and chemical properties of the activated carbons are strongly dependent on the precursor materials and method of

[a]*Solid State Ionics and Energy Devices Laboratory, Department of Physics, Bharathiar University, Coimbatore-641046, Tamil Nadu, India. E-mail: selvankram@buc.edu.in*

[b]*Faculty of Applied Chemical Engineering, Chonnam National University, Gwangju 500-757, Korea*

[c]*Nuclear Agriculture and Biotechnology Division, Bhabha Atomic Research Centre, Trombay, Mumbai-400085, India*

† Electronic supplementary information (ESI) available. See DOI: 10.1039/c2ta00210h

synthesis.[14] Previously, activated carbons have been prepared from various waste biomasses such as banana fibres,[15a] corn grains[15b] and sugarcane bagasse.[15c]

Very recently, an interesting approach has been reported wherein redox additives or mediators are introduced into the electrolyte to substantially enhance the capacitance *via* redox reaction between the electrode and electrolyte. Notably, Su *et al.* have reported that the capacitance of Co–Al LDH (layered double hydroxide) electrode was improved through addition of 0.1 M $K_3Fe(CN)_6$ or 0.1 M $K_4Fe(CN)_6$ into 1 M KOH solution. The mixed electrolytes of 1 M KOH + 0.1 M $K_3Fe(CN)_6$ or 1 M KOH + 0.1 M $K_4Fe(CN)_6$ exhibited an increased capacitance values of 712 and 317 F g^{-1} which is higher than for 1 M KOH solution (226 F g^{-1}).[16] Recently, Roldan *et al.* have reported an increase in capacitance from 72 (1 M H_2SO_4) to 220 F g^{-1} by introduction of hydroquinone/quinone into 1 M H_2SO_4 solution.[17a] Similarly, CNT based capacitance of 17 F g^{-1} (1 M H_2SO_4) was raised to 50 F g^{-1} by introducing indigo carmine in 1 M H_2SO_4.[3] More recently, the capacitance of MnO_2 was increased from 44.87 to 325.24 F g^{-1} *via* introduction of *p*-phenylenediamine into KOH.[18a] Also, *m*-phenylenediamine added to KOH raised the capacitance of the carbon from 36.43 to 78.01 F g^{-1}.[19a] Based on these reports it can be concluded that the redox additives or compounds can increase the original capacitance of the supercapacitor material by two- to three-fold. Herein, we attempted to enhance the capacitance of a carbon based supercapacitor *via* addition of KI into 1 M H_2SO_4 electrolyte since iodide (I^-) can produce redox pairs such as $3I^-/I_3^-$, $2I^-/I_2$, $2I_3^-/3I_2$ and I_2/IO_3^- during the electrochemical process.[20] Moreover, the ionic size of I^-, I_3^- (I_3^- solvated by 4 water molecules), I_5^- and IO_3^- (IO_3^- solvated by 3 water molecules) are 0.39 nm, 0.63 (1.8) nm, 1.2/1.26 nm (shorter/longer length) and 0.57 (1.4) nm, respectively. Due to the small ionic sizes, the ions can easily access the micropores and small mesopores of the porous electrode.[21a] To our knowledge, there is no previous report on I^- addition to an acidic electrolyte for supercapacitor materials. In this report, the activated carbon was derived from biomass of *Eichhornia crassipes* by $ZnCl_2$ activation at different carbonization temperatures (500, 600, 700, 800 and 900 °C). First, the best electrochemically active electrode was optimised through CV, EIS and GCD techniques in 1 M H_2SO_4 electrolyte. Subsequently, the symmetric supercapacitor was fabricated using the optimized electrode and studied for its electrochemical performances in 1 M H_2SO_4. Then the capacitive/energy performance was further improved *via* addition of 0.08 M KI into 1 M H_2SO_4 electrolyte, and also compared with 1 M H_2SO_4 + 0.08 M KBr and 1 M Na_2SO_4 + 0.08 M KI solutions.

2 Experimental methods and materials

2.1. Preparation and characterization of ACs

Eichhornia crassipes (common water hyacinth) was collected from Periyakulam Lake (Coimbatore city, Tamil Nadu, India) and was used as a precursor for the activated carbon. The activated carbon was prepared as follows based on our previous work.[21b] First, the *Eichhornia crassipes* was fragmented into small pieces and dried in sunlight. Subsequently, the dried precursor was pulverized and pre-heated at 200 °C to remove moisture. Then the desired amount of pre-heated sample was activated using 10% of $ZnCl_2$ for 24 h. Subsequently it is carbonized at various temperatures: 500 °C (Zn-1), 600 °C (Zn-2), 700 °C (Zn-3), 800 °C (Zn-4) and 900 °C (Zn-5) for 2 h under Ar atmosphere. Further, the carbonized samples were washed with distilled water and desired amount of 1 M HCl and finally dried at 100 °C overnight.

The prepared ACs were characterised by XRD (X'Pert PRO PANalytical X-ray Diffractometer) and Raman measurement (Jobin-Yvon ISA T 64000). FTIR spectra of the ACs were recorded using a Bruker tensor 27. The microscopic structure of the ACs were observed by scanning electron microscopy (SEM) (Quanta 200 ESEM, FEI, USA). The surface area, pore size and pore distribution of the ACs was carried out using nitrogen absorption–desorption experiments at 77 K (Micromeritics ASAP 2010 surface area analyser) and calculated by the BET and BJH method, respectively. The electrochemical measurements were performed at room temperature using Bio-Logic SP150 instrumentation. For the three-electrode system, Pt wire and Ag/AgCl were used as counter and reference electrodes, respectively. Here, CV and GCD tests were performed in the potential range of −0.2 to 0.8 V at various scan rates (5–50 mV s^{-1}) and current densities from 2 to 10 mA cm^{-2} respectively. EIS measurements were performed by applying an AC voltage with 10 mV amplitude in the frequency range of 10 mHz to 1 MHz at open circuit voltage (OCV).

2.2 Fabrication of AC electrodes and symmetric supercapacitors

The working electrodes was fabricated as follows; typically, the activated carbon (20 mg), carbon black (2 mg) and poly(vinylidene fluoride) (PVDF, 2 mg) were mixed and dispersed in 0.4 ml of *N*-methyl-2-pyrrolidone (NMP) to produce a homogenous slurry. Then 12 μl of the resulting slurry was coated onto a

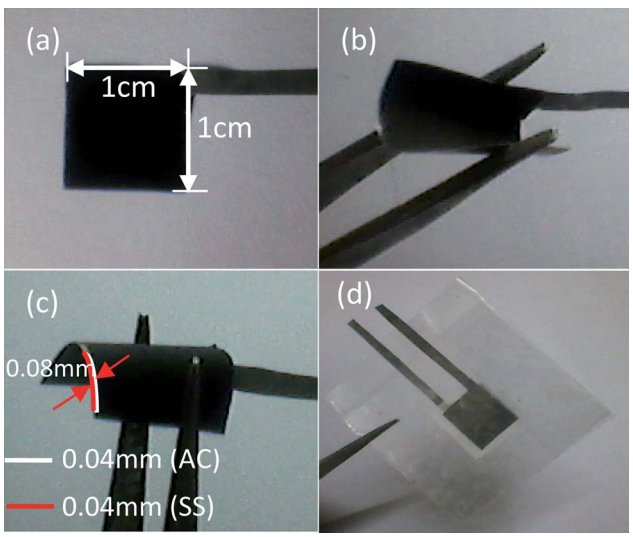

Fig. 1 Prepared AC electrode (a) at normal, (b and c) flexible condition and (d) assembled supercapacitor.

0.04 mm thick flexible (Fig. 1a–c) stainless steel sheet (1 cm × 1 cm). Finally, the fabricated electrodes were dried at 50 °C in an oven for overnight. The loaded activated carbon was calculated to be ~0.6 mg (excluding carbon black and PVDF mass) on each electrode and measured thickness of the coated AC was found to be 0.04 mm by using a screw gauge.

The symmetric supercapacitor (SC) was assembled using the prepared activated carbon electrode, separated by a polypropylene sheet immersed with 1 M H_2SO_4, 1 M H_2SO_4–0.08 M KI, 1 M H_2SO_4–0.08 M KBr or 1 M Na_2SO_4–0.08 M KI. The assembly of the supercapacitor was successfully completed in air at room temperature (Fig. 1d). However, for commercialisation these fabrication methods need to be improved.

3 Results and discussion

3.1 Porosity, chemical and physical characterisation of ACs

The N_2 adsorption–desorption isotherms, pore size distributions and the relation between the pore size and adsorbed pore volumes are shown in Fig. 2 for the prepared activated carbons. Type IV isotherms are observed in Fig. 2a which indicates the presence of different pore sizes from micro- to macropores. The increasing adsorbed volume at low pressure (~0–0.2) is related to micropores, the desorption hysteresis at medium relative pressure (~0.2–0.9) reveals the presence of mesopores and the small tails at a relative pressure near to 1.0 (>0.9) reveals the presence of macropores.[22,23] The obtained Brunauer–Emmett–Teller (BET) surface areas, total pore volumes and average pore sizes are given in Table 1. Mesoporous and microporous surface areas and pore sizes of ACs are obviously increased with carbonization temperatures especially from 600 °C. Among the prepared ACs, Zn-5 shows the high surface area (579.94 $m^2\ g^{-1}$) and pore volume (0.34 $cm^3\ g^{-1}$) as well as the best pore size of 2.33 nm. Fig. 2b shows the pore size distribution of the ACs which is calculated by the Barrett–Joyner–Halenda (BJH) method. The maximum peak is observed for Zn-5 (Fig. 2c) centred at 3.7 nm which infers that majority of pores are mesopores. Moreover, Zn-5 displays the largest adsorbed volume (Fig. 2d) which indicates a higher surface area, larger pore volume, with better pore size.

Fig. 3a and b show representative SEM images of Zn-1 and Zn-5 and show the presence of porous morphology without any particular shape. This porous morphology plays an important role in electrochemical performance because the electrolyte ions easily pass through the porous structure leading to good capacitance and improved wettability of the electrode.

The presence of surface functional groups was identified through FTIR (Fig. 4). The bands at 1100–1390 cm^{-1} is attributed to C–O stretching vibration in phenols, alcohols, acids, ethers and esters. The observed bands at 1560–1577 cm^{-1} are ascribed to C=O (corresponding to carbonyl, carboxyl or quinone groups) stretching vibrations. Bands at 3400–3100 and 1000–1038 cm^{-1} correspond to stretching vibration of O–H in hydroxyl or carboxyl groups, respectively. Weak bands at 1560–1577, 1000–1038 and 3400–3100 cm^{-1} at higher carbonization temperature suggest decomposition of oxygen and occurrence of dehydration.[14] This removal of functional groups is indirectly observed from EDAX analysis (for details see Fig. S1†). EDAX shows that the Zn-1 sample contains 76.05 wt% (86.38 at%) of carbon whereas Zn-5 has 84.85 wt% (90.18 at%) of carbon. This enhancement of carbon percentage may be due to the elimination of functional groups or decreasing residuals at higher carbonization temperature.

The typical XRD pattern of ACs is shown in Fig. 4b. The broad carbon peak is observed between 20 and 30° which corresponds to the (002) plane. This indicates that the ACs

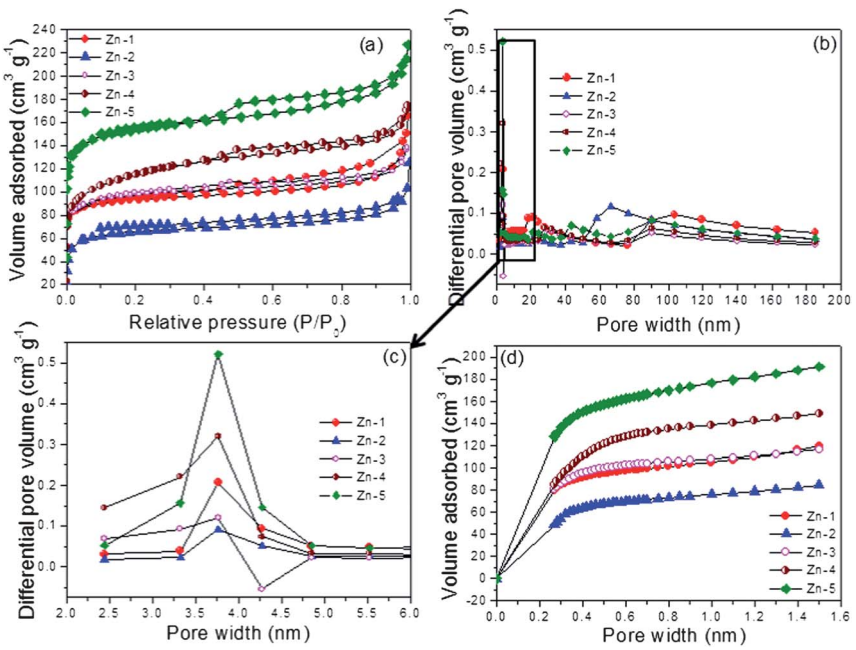

Fig. 2 (a) N_2 adsorption–desorption isotherms, (b and c) pore size distributions and (d) pore widths *vs.* volume adsorbed of Zn-1, Zn-2, Zn-3, Zn-4 and Zn-5.

Table 1 Surface area, pore volume, pore size and capacitance of the prepared activated carbons

Sample	S_{BET}/m^2 g^{-1}	V_p[a]/cm^3 g^{-1}	d_p[a]/nm	$S_{micropore}$[b]/m^2 g^{-1}	$V_{micropore}$[b]/cm^3 g^{-1}	C_{sp}[c]/F g^{-1}	C_{sp}[d]/F g^{-1}
Zn-1	353.83	0.24	2.70	456.61	0.14	409	—
Zn-2	248.11	0.16	2.58	280.09	0.10	374	—
Zn-3	367.54	0.21	2.31	459.82	0.16	436	—
Zn-4	412.04	0.27	2.58	485.71	0.20	405	—
Zn-5	579.94	0.34	2.33	732.25	0.24	530	472

[a] Total pore volume calculated at $P/P_0 = 0.99$ and average pore diameter from BET method. [b] Microporous surface area and micropore volume from *t*-plot method. [c] Maximum specific capacitance calculated at 2 mA cm^{-2} from three-electrode system. [d] Maximum specific capacitance calculated at 2 mA cm^{-2} from two-electrode system.

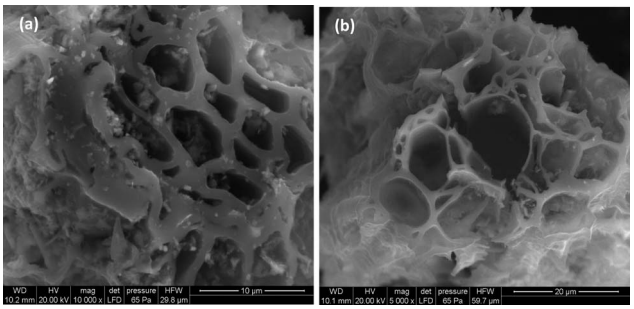

Fig. 3 SEM images of (a) Zn-1 and (b) Zn-5.

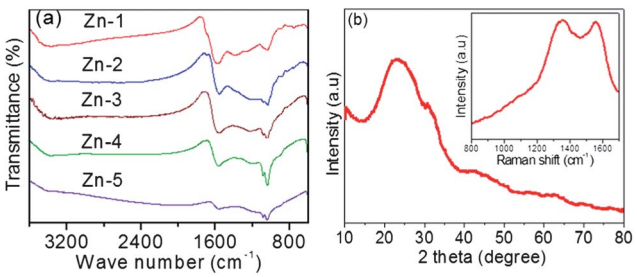

Fig. 4 (a) FTIR spectra of ACs, (b) XRD pattern and Raman spectra (inset) of Zn-5.

contain small disordered structures of aromatic sheets.[14] Raman studies provide further information of microstructures and confirmation of activated carbon. A representative Raman spectrum of Zn-5 is shown in Fig. 4b (inset). There are two peaks; one around 1348 cm^{-1} corresponds to sp^3 configuration of a disordered D-band which is due to the carbon-dangling bond vibrations and thus confirms the presence of dangling bond carbon atoms such as carbon–oxygen.[14] The band at around 1577 cm^{-1} corresponds to sp^2 configuration of graphitic (G-band) carbon which is due to C=C stretching vibration.

3.2 Electrochemical properties of AC electrodes (three-electrode system)

EIS is an informative techniques to study the conductive properties and charge storage kinetics of electrode materials. Fig. 5a shows the Nyquist plot of all the prepared AC electrodes. At low frequency (Fig. 5a), the large and small tails reveal the slow and quick access of ions into the porous electrode. Additionally, about 45° inclined line and vertical lines close to 90° reveals the non-ideal (frequency dependence of ionic diffusion – Warburg resistance) and ideal capacitive nature of the electrodes.[24] The observed semicircle at high frequency (Fig. 5b) shows the presence of possible pseudo-capacitive interaction of all the electrodes. The diameter of the semicircle decreases with increasing carbonization temperature and indicates the decreasing pseudo-capacitive interaction, because it occurs mainly due to the presence of functional groups on the AC. The smallest semicircle is observed for Zn-5 among the ACs which signifies its lower intrinsic resistance.[9,25]

Fig. 5c shows the relation between the frequency and phase angle. Interestingly, the phase angle changes from −58° to −85° from Zn-1 to Zn-5, which reveals the decrease in intrinsic resistance with increasing carbonization temperature from 500 to 900 °C and further confirms the change of capacitive behavior from pseudo-capacitive to EDLC behaviour. This decreasing intrinsic resistance is due to the reduction of functional groups with increasing carbonization temperature. Based on previous reports[9,24] it can be concluded that higher intrinsic resistance is exhibited by a more pseudo-capacitive nature of the electrodes during the electrochemical process. Fig. 5d clearly shows that the frequency dependent impedance is decreased with increasing carbonization temperature, which signifies the improved conductivity of the AC electrode. Generally, the frequency independent, *i.e.*, high frequency region suggests capacitive behaviour which is associated with ionic diffusion in mesopores.[26a] Here, the Zn-5 electrode reaches the frequency independent impedance at very low frequency, the order being Zn-5 (~3.5 Hz) < Zn-4 (~7.8 Hz) < Zn-3 (~25.4 Hz) < Zn-2 (~121.4 Hz) < Zn-1 (266.7 Hz), demonstrating that the Zn-5 electrode has better ionic diffusion than the other AC electrodes.

The typical CV curves at 5 mV s^{-1} of all AC electrodes are shown in Fig. 6a. All the electrodes except Zn-1 and Zn-2 exhibit quasi-rectangular behaviour which suggests that their capacitance predominantly arises from combination of electrical double layer capacitance (EDLC) *via* accumulation of charges at the electrode/electrolyte interface and pseudo-capacitance through reverse redox reaction between oxygen functionalities such as C=O and H^+.[14] The Zn-1 and Zn-2 electrodes show more non-ideal capacitive curves due to the possible presence of more functional groups due to the low carbonization temperature, resulting in poor electrical conductivity. Generally, capacitance

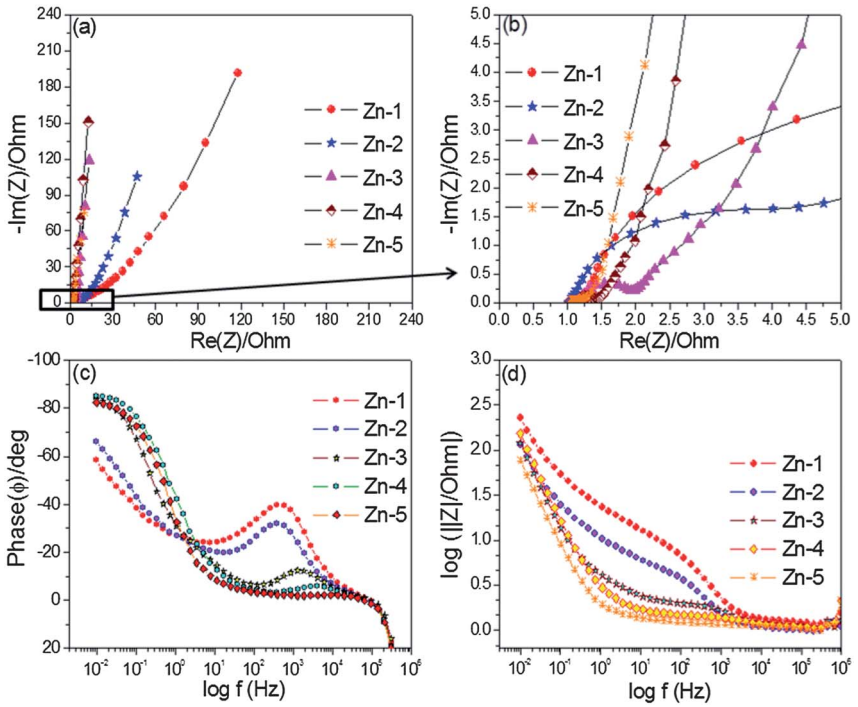

Fig. 5 (a and b) EIS, (c) log *f vs.* phase angle and (d) log *f vs.* log|*Z*| spectra of ACs.

of carbon based materials is mainly enhanced by redox reactions due to the presence of functional groups. Among the AC electrodes, Zn-5 shows the largest current area in CV curves so it could deliver a higher capacitance even with increasing scan rate; the CV curve maintains its original shape even up to 50 mV s^{-1} which indicates good access of charges or ions into the bulk of the porous material (see Fig. S3†). This excellent electrochemical performance of Zn-5 may be due to the higher surface area, and larger pore volume with pore size of 2.33 nm, than the other ACs. The excellent characteristics are further substantiated by calculating the mean areal capacitance from the relation between the discharge current and scan rate (Fig. 6b).[26b] The

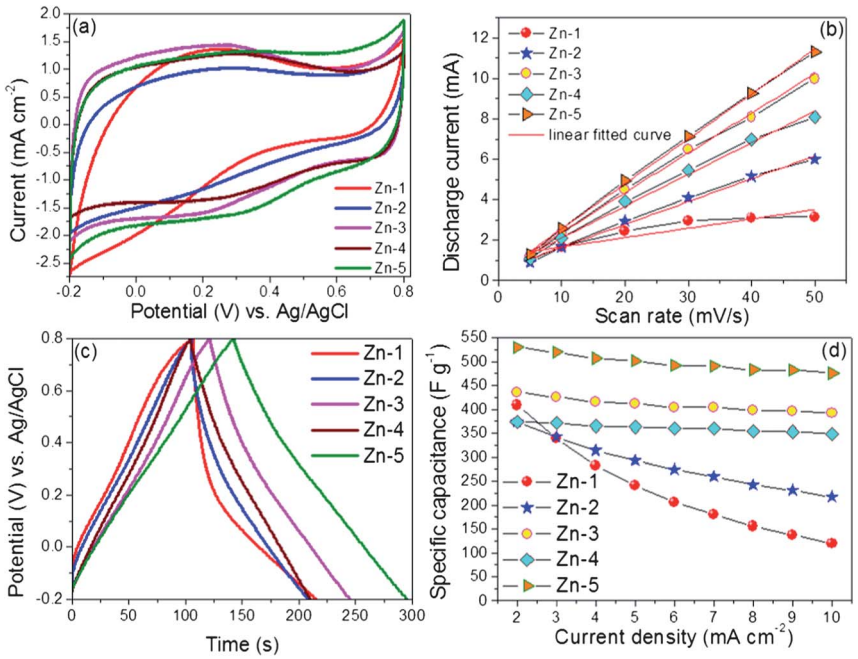

Fig. 6 (a) CV curves at 5 mV s^{-1}, (b) scan rate *vs.* discharge current, (c) galvanostatic charge–discharge curves at 2 mA cm^{-2} and (d) specific capacitance *vs.* current density of ACs.

maximum mean areal capacitance is obtained for Zn-5 (0.22 F cm^{-2}) when compared with Zn-1 (0.05 F cm^{-2}, Zn-2 (0.11 F cm^{-2}), Zn-3 (0.19 F cm^{-2}) and Zn-4 (0.15 F cm^{-2}). In addition better linear current behaviour is observed for Zn-5 due to better electrolyte ion diffusion behaviour, even at high scan rates.[26b] On the other hand, a deviation of linear current behaviour is obtained with increasing scan rate for the remainder of the samples, that indicates the limits of electrolyte ion diffusion into the electrodes.

Galvanostatic charge–discharge (GCD) cycling was carried out using three-electrode systems for all ACs at different current densities (2–10 mA cm^{-2}) and representative GCD curves (2 mA cm^{-2}) are shown in Fig. 6c. Zn-1 and Zn-2 electrodes provide more non-linear and non-ideal GCD curves, which further confirms the existence of pseudo-capacitive behaviour.[27,28] Also, both these electrodes exhibit a larger *IR* drop, with the observed *IR* drop in the order of Zn-1 (0.1 V) < Zn-2 (0.04 V) < Zn-3 (0.02 V) < Zn-4 (0.014 V) < Zn-5 (0.006 V). Subsequently, the internal resistance (ESR) of the electrode was calculated[26b] using ESR = $V_{IR}/2I$; where, 'V_{IR}' is the *IR* drop and '*I*' is the discharge current. A low internal resistance of 1.5 Ω cm^2 is obtained for Zn-5, while values of 25, 10, 5 and 3.5 Ω cm^2 are measured for Zn-1, Zn-2, Zn-3 and Zn-4, respectively. Fig. 6d shows the calculated specific capacitance as a function of current density for all the electrodes. The capacitance of the ACs progressively decreased with increasing current density because of their fast ionic motion into/out of the pores of the AC electrode during the charge–discharge process. Also a lower number of ions contribute to charge storage with the occurrence of less ionic interaction with oxygen functionalities for redox reaction at higher current density. The specific capacitance (C_{sp}) of the electrodes is calculated using the following equation,[29]

$$C_{sp} = \frac{I}{m(dv/dt)} \quad (1)$$

where, *I* is the discharge current density, d*v*/d*t* is the average slope of the discharge curve and *m* is the mass of the active material in the electrode. Among the electrodes, Zn-5 electrode delivered a maximum capacitance of 530 F g^{-1} which was higher than the others (409 F g^{-1} for Zn-1, 374 F g^{-1} for Zn-2, 436 F g^{-1} for Zn-3 and 405 F g^{-1} for Zn-4). It can be concluded that the observed high capacitance of Zn-5 may be due to its higher surface area, larger pore volume, with pore size of 2.33 nm, as well as low ionic diffusion resistance and low internal resistance.

3.3 Performance of symmetric supercapacitors (two-electrode system)

Based on the above studies, the Zn-5 electrode exhibits better electrochemical properties and higher specific capacitance. Hence, a symmetric supercapacitor was fabricated using Zn-5 electrode in AC|H_2SO_4|AC (AH) configuration. In order to further enhance the specific capacitance of the AH configuration, KI + H_2SO_4 electrolyte was investigated in the AC|H_2SO_4–KI|AC (AHK) system. For comparison, the AC|H_2SO_4–KBr|AC (AHB) and AC|Na_2SO_4–KI|AC (AHNa) systems were also studied.

Fig. 7a and b shows the CV (at 5 mV s^{-1}) and GCD (2 mA cm^{-2}) curves of AH and AHK supercapacitors. The CV curve of AH shows ideal capacitive behaviour *i.e.*, rectangular, being retained even at a high scan rate of 50 mV s^{-1} (Fig. 7c). In contrast, the AHK system shows non-ideal capacitive behaviour but covers more current area due to the larger number of possible redox reactions between the pairs of $3I^-/I_3^-$, $2I^-/I_2$, $2I_3^-/3I_2$ and I_2/IO_3^-, with the corresponding redox equations given below:[20]

$$3I^- \leftrightarrow I_3^- + 2e^- \quad (2)$$

$$2I^- \leftrightarrow I_2 + 2e^- \quad (3)$$

$$2I_3^- \leftrightarrow 3I_2 + 2e^- \quad (4)$$

$$I_2 + 6H_2O \leftrightarrow 2IO_3^- + 12H^+ + 10e^- \quad (5)$$

At high scan rate, the AHK (Fig. 7d) exhibits prominent redox peaks when compared with low scan rate that infers the better electrochemical reversibility of the SC. Redox peak shifting was observed with increasing scan rate which indicates the occurrences of better electrochemical and redox process between the electrode/electrolyte interface. Moreover, AHK covering a larger current area than AH, leads to a higher capacitance. This result indicates that the addition of KI into H_2SO_4 improved the capacitive behaviour *via* pseudo-capacitive reactions.

This was further substantiated by the GCD technique (Fig. 7b and f); a Faradaic plateau (non-ideal triangle) was observed for AHK due to the voltage dependent redox reactions. On the other hand a linear charge–discharge (CD) curve is obtained for AH because of the EDLC behaviour. From this, it can be confirmed that the iodine ions are responsible for this obtained high capacitance through this pseudo-capacitive behaviour. The cell capacitance (C_{Cell}), specific capacitance of the electrode (C_{sp}), energy density (*E*) and power density (*P*) of the SCs are calculated using the following equations;[29,30]

$$C_{Cell} = \frac{I}{M(dv/dt)};\ C_{sp} = 4C_{Cell} \quad (6)$$

$$E = \frac{I\int V(t)dt}{M} \quad (7)$$

$$P = E/t \quad (8)$$

where, *I* is the discharge current density, d*v*/d*t* is average slope of the discharge curve, $\int V(t)dt$ is the integral area of discharge curve, *t* is discharge time and *M* is the total mass of the active material in both electrodes. Fig. 7g and h depict the variation of specific capacitance with respect to current density and Ragone plot of AH and AHK, respectively. The AHK system delivered the maximum specific capacitance and energy density of 912 F g^{-1} at 2 mA cm^{-2} and 19.04 W h kg^{-1} at 224.43 W kg^{-1} which is nearly twice the specific capacitance and energy density of AH (472 F g^{-1}, 9.5 W h kg^{-1}) and comparable with previous reports (see Table 2). In order to further substantiate the contribution of

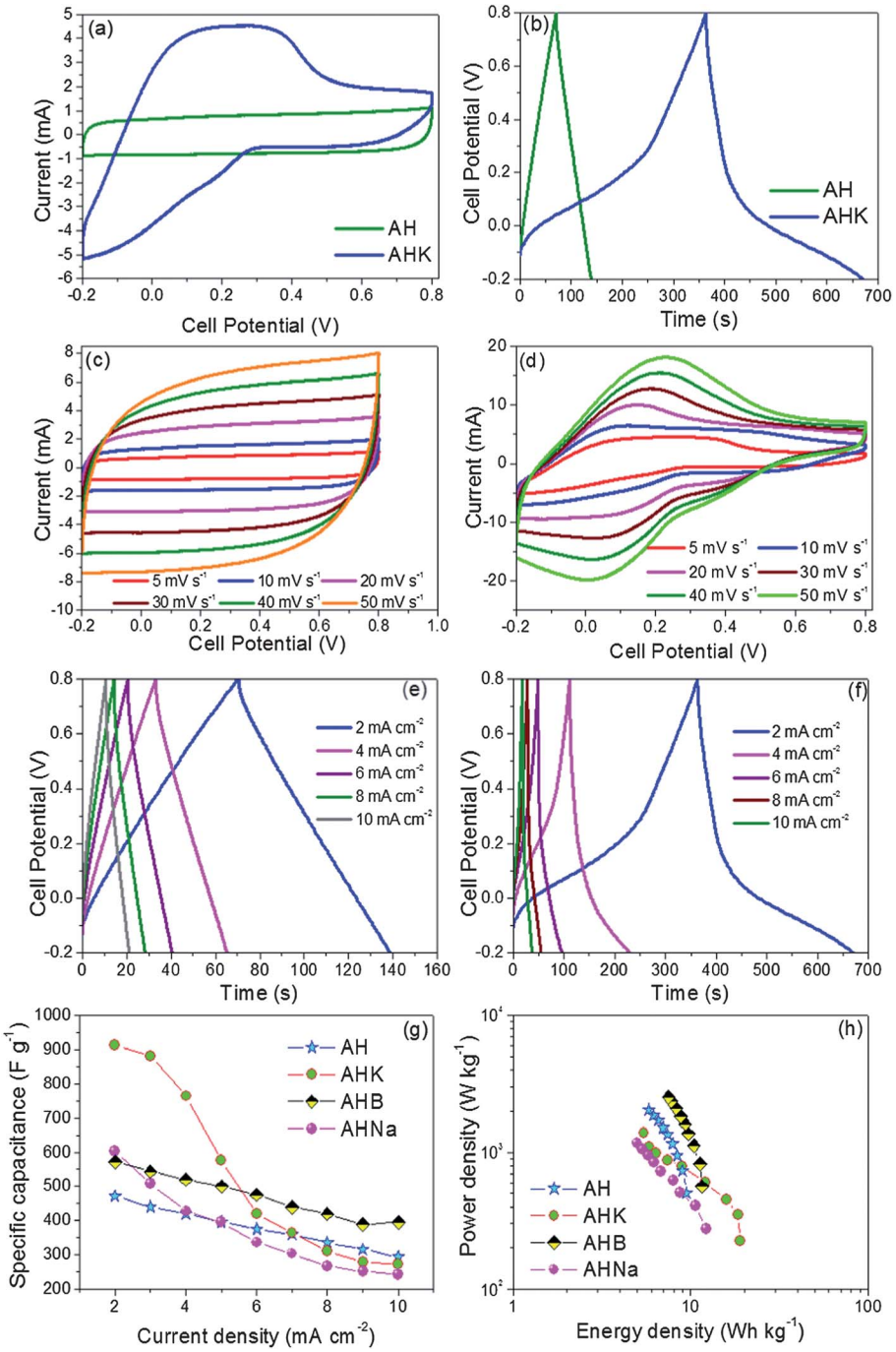

Fig. 7 CV curves at (a) 5 mV s^{-1} and (b) GCD curves at 2 mA cm^{-2} for AH and AHK; (c and d) CV curves at 5–50 mV s^{-1} and (e and f) GCD curves at 2, 4, 6, 8 and 10 mA cm^{-2} for AH and AHK; (g) specific capacitance *vs.* current density and (h) Ragone plots for AH, AHK, AHB and AHNa.

iodine ions in H_2SO_4 electrolyte to obtain the high specific capacitance, two different electrolyte systems, KBr + H_2SO_4 (AHB) and KI + Na_2SO_4 (AHNa), were also investigated. The typical CV curves of AHB and AHNa are given in Fig. 8a. AHNa shows the same redox peaks as for AHK but covers less current area. In AHB, the Br^-/Br_3^- pair (see eqn (9)) is responsible for the redox peaks.[31]

$$3Br^- \leftrightarrow Br_3^- + 2e^- \quad (9)$$

Overall, AHK covers the larger current area in CV which leads to its higher capacitance relative to AH, AHB and AHNa, which are in the order of AH < AHB < AHNa < AHK (Fig. S6†). Similarly, the charge–discharge curves also shows non-ideal triangle behaviour for both AHNa and AHB (Fig. 8b). Further, the higher discharge time observed for AHK than AH, AHNa and AHB, indicates the higher capacitance nature (Fig. S6†). The calculated specific capacitance and energy density for AHB and AHNa are 572 F g^{-1}, 11.6 W h kg^{-1} and 604 F g^{-1}, 12.3 W h kg^{-1}

Table 2 Comparison of specific capacitance and energy density with different reported values

Electrode material	Electrolyte	C_{sp}/F g^{-1}	Conditions	Energy density/W h kg^{-1}	Ref.
MWCNTs	H_2SO_4 + indigo carmine	50	0.88 mA cm^{-2}	1.7	3
Co–Al layered double hydroxide	KOH + $K_3Fe(CN)_6$	712	2 A g^{-1}	—	16
	KOH + $K_4Fe(CN)_6$	317	2 A g^{-1}	—	16
Activated carbon (commercial)	H_2SO_4 + hydroquinone	220[a]	2.65 mA cm^{-2}	30.6	17*a*
		901	2.65 mA cm^{-2}	31.3	17*b*
Activated carbon (commercial)	H_2SO_4 + $CuSO_4$ + $FeSO_4$	223 mA h g^{-1}	—	—	17*c*
MnO_2	KOH + *p*-phenylenediamine	325.24	1 A g^{-1}	10.12	18*a*
Activated carbon (commercial)	KOH + *p*-phenylenediamine	605.22	1 A g^{-1}	19.86	18*b*
Activated carbon (commercial)	KOH + *m*-phenylenediamine	78	0.5 A g^{-1}	9.99	19*a*
MWCNTs	H_2SO_4 + methylene blue	279	0.88 mA cm^{-2}	—	19*b*
Activated carbon (from *Eichhornia crassipes*)	H_2SO_4–PVA + hydroquinone	941	1 mA cm^{-2}	20	21*b*
Activated carbon (form petroleum coke)	1-Ethyl-3-metylmidazolium tetrafluoroborate + Cu^{2+}	225	1 mA cm^{-2}	45	35
Activated carbon (commercial)	H_2SO_4 + lignosulfonates	178	0.1 A g^{-1}	—	36*a*
Activated carbon (commercial)	KOH–PVA + KI	236.9	800 mA g^{-1}	15.34	36*b*
Activated carbon (commercial)	H_2SO_4–PVA + *P*-benzenediol	474.29	0.83 A g^{-1}	11.31	36*c*
Activated carbon (from *Eichhornia crassipes*)	H_2SO_4 + KI	912	2 mA cm^{-2}	19.04	[b]
	H_2SO_4 + KBr	572	2 mA cm^{-2}	11.6	[b]
	Na_2SO_4 + KI	604	2 mA cm^{-2}	12.3	[b]

[a] Cell capacitance. [b] Present work.

respectively. AHNa shows a better specific capacitance and energy density than AH, AHB, but lower than AHK. AHNa delivered lower specific capacitance and energy density than AHK because the surface functional groups are not involved in the redox reaction in neutral electrolytes (*i.e.*, pH is neutral). The acidic medium with H^+ ions can be involved in the redox reactions with surface functional groups resulting in improved capacitance.[32] This result is in good agreement with the CV test (Fig. S6†). So, the combination of redox reactions of H^+ ions and I^- ions in AHK lead to better SC properties than for AHNa and AHB. In addition, the capacitance of the SCs decreases with current density which may be due to the low number of electrolyte ions with partial occurrence of redox reactions on the electrode surface.

EIS measurements were carried out for AH and AHK and corresponding Nyquist plots are shown in Fig. 9a. It is seen that a semicircle was observed at high frequency for both SCs and this result corresponds to the internal resistance of the SCs. Subsequently, AH exhibits a 45° inclined line at medium frequencies which confirms the presence of a redox reaction process. In addition, at lower frequency the Warburg line was noted for AH that signifies the diffusive resistance in electrode pores and diffusion of ions in the host materials. The solution resistance (R_s) and charge transfer resistance (R_{ct}) in the electrode was calculated from the intercept point of semicircle at the *x*-axis at higher value and high to low frequency. The calculated solution resistances of the AH and AHK are 1.2 Ω and 2.4 Ω whereas the measured charge transfer resistances are 1.2 Ω and 0.7 Ω, respectively. This change in solution resistance is due to the addition of KI. A similar observation was already reported for indigo carmine added to 1 M H_2SO_4.[3] AHK provides lower charge transfer resistance in the electrode compared to AH and cited reports.[18a,b] In addition, the AHK demonstrates a smaller diameter semicircle which also reveals the good ionic conductivity at the electrode/electrolyte interfaces.

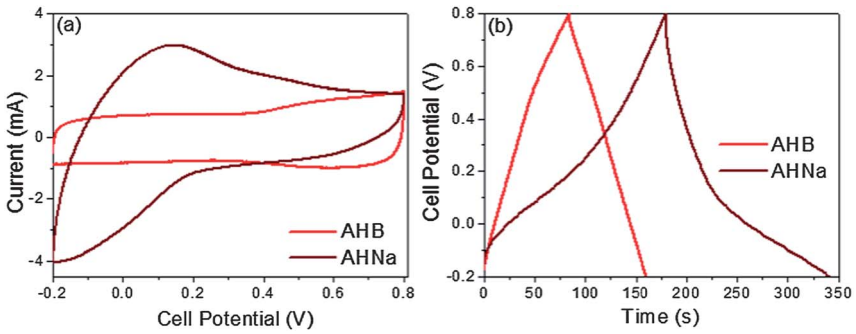

Fig. 8 (a) CV curves at 5 mV s^{-1} and (b) galvanostatic charge–discharge curves at 2 mA cm^{-2} of AHB and AHNa.

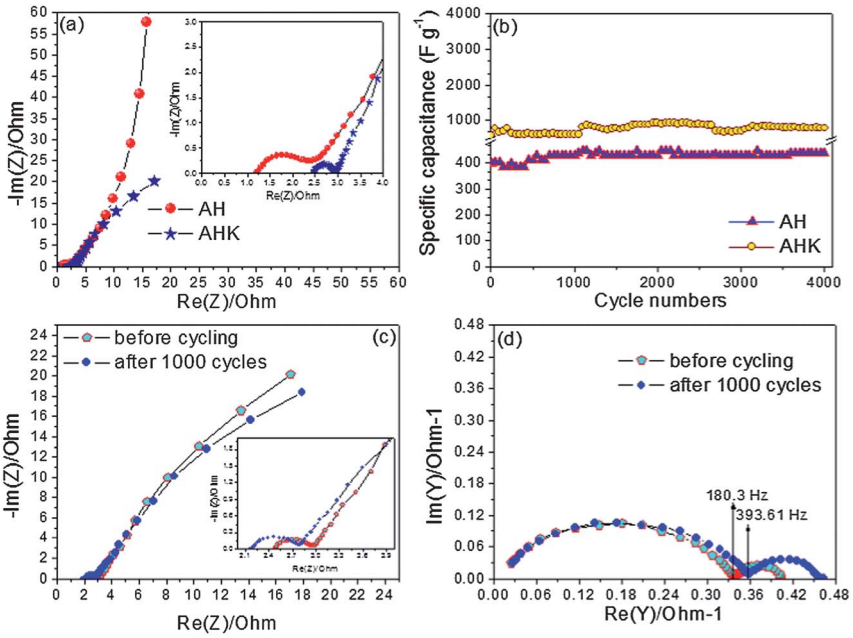

Fig. 9 (a) Nyquist plot of AH and AHK, (b) cycle life of AH and AHK, (c) Nyquist and (d) admittance plots before cycling and after 1000 cycles of AHK.

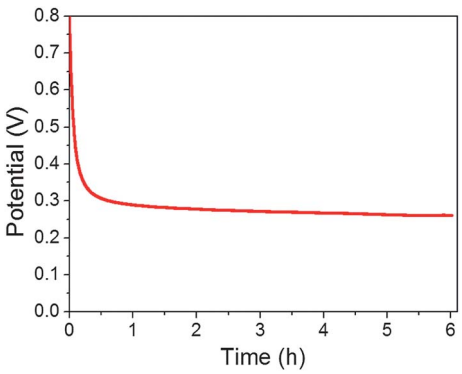

Fig. 10 Self-discharge of AHK.

For practical applications, an SC should have extensive cycle stability. The cycle stability of AH and AHK were evaluated by galvanostatic charge–discharge test at 5 mA cm^{-2} and results are shown in Fig. 9b. AH shows an increasing specific capacitance from 396 to 413 F g^{-1} after ~500 cycles and also after 1400 cycles it maintains a constant specific capacitance of 438 F g^{-1} up to 4000 cycles. Here, the increasing specific capacitance is because of the removal of oxygen functional groups. This phenomenon is well documented[33] and is further substantiated from EIS measurements (for details see Fig. S8†). A similar behaviour is also seen for AHK with the specific capacitance of AHK increasing from 576 (at first cycle) to 781 F g^{-1} (after 4000 cycles). Here the increase in capacitance is possible due to a couple of reasons; the removal of oxygen functional groups, as above, but also improved access of I^- ions into the pores of the electrode after a number of cycles. Fig. 9c and d show Nyquist plots of impedance and admittance spectra of AHK before and after 1000 cycles. After 1000 cycles the solution resistance and charge transfer resistance in the electrode decreased from 2.3 Ω to 2.18 Ω and from 0.7 Ω to 0.6 Ω which is conceivably due to the removal of oxygen functional groups with repeated cycling (same behaviour as for AH, for details see ESI†). Moreover, the knee frequency of the AHK is raised after 1000 cycles from 180.3 Hz to 393.6 Hz which also infers the improved performance of the supercapacitor.[34]

The self-discharge behaviour of AHK was studied by charging it to 0.8 V. The voltage drop was then recorded at open circuit voltage with respect to time. In the self-discharge curve (Fig. 10) it is seen that for the first 0.5 h a sharp voltage drop (up to ~0.32 V) is observed. However, after 0.5 h an almost constant voltage of 0.263 V is maintained and is better than in previous reports.[37a,b]

4 Conclusion

In summary, an activated carbon was prepared with surface area of 579.94 m^2 g^{-1} and pore size of 2.33 nm by $ZnCl_2$ activation at 900 °C. This biomass derived activated carbon supercapacitor (SC) delivered a specific capacitance and energy density of 472 F g^{-1} and 9.5 W h kg^{-1} in aqueous solution (1 M H_2SO_4). Expectedly, after adding I^- additive in the form of 0.08 M KI the specific capacitance and energy density of the SC increases nearly two-fold *i.e.*, 912 F g^{-1} and 19.04 W h kg^{-1}, with excellent cycle stability over 4000 cycles. In comparison, 0.08 M KBr–1 M H_2SO_4 and 0.08 M KI–1 M Na_2SO_4 electrolytes delivered a lower specific capacitance and energy density of 572 F g^{-1}; 11.6 W h kg^{-1} and 604 F g^{-1}; 12.3 W h kg^{-1}, respectively. Based on these results, it is hoped that the combination of biomass derived activated carbon and halogen additive–aqueous electrolyte (1 M H_2SO_4–0.08 M KI) can facilitate

improved capacitance/energy of supercapacitors to enable practical application in the near future.

Acknowledgements

The authors gratefully thank the financial support from Department of Atomic Energy-Board of Research in Nuclear Sciences (DAE-BRNS), Government of India (no. 2010/37P/46/BRNS/1443).

References

1 G. Pognon, T. Brousse and D. Belanger, *Carbon*, 2011, **49**, 1340.
2 Q. Wu, Y. Sun, H. Bai and G. Shi, *Phys. Chem. Chem. Phys.*, 2011, **13**, 11193.
3 S. Roldan, Z. Gonzalez, C. Blanco, M. Granda, R. Menendez and R. Santamaria, *Electrochim. Acta*, 2011, **56**, 3401.
4 K. R. Prasad and N. Munichandraiah, *Electrochem. Solid-State Lett.*, 2002, **5**, A271.
5 K. Fic, G. Lota and E. Frackowiak, *Electrochim. Acta*, 2010, **55**, 7484.
6 (*a*) X. Fan, Y. Lu, H. Xu, X. Kong and J. Wang, *J. Mater. Chem.*, 2011, **21**, 18753; (*b*) K. Zhang, L. L. Zhang, X. S. Zhao and J. Wu, *Chem. Mater.*, 2010, **22**, 1392; (*c*) Z. Lei, Z. Chen and X. S. Zhao, *J. Phys. Chem. A*, 2010, **114**, 19867.
7 D. H. Jurcakova, M. Seredych, G. Q. Lu and T. J. Bandosz, *Adv. Funct. Mater.*, 2009, **19**, 438.
8 L. Zhao, L. Z. Fan, M. Q. Zhou, H. Guan, S. Qiao, M. Antonietti and M. M. Titirici, *Adv. Mater.*, 2010, **22**, 5202.
9 D. Hulicova, M. Kodama and H. Hatori, *Chem. Mater.*, 2006, **18**, 2318.
10 D. H. Jurcakova, A. M. Puziy, O. I. Poddubnaya, F. S. Garcia, J. M. D. Tascon and G. Q. Lu, *J. Am. Chem. Soc.*, 2009, **131**, 5026.
11 D. W. Wang, Z. G. Chen, G. Q. Li and H. M. Cheng, *Chem. Mater.*, 2008, **20**, 7195.
12 B. Viswanathan, P. I. Neel and T. K. Varadarajan, *Method of Activation and Specific Application of Carbon Materials*, National Centre for Catalysis Research-IIT Madras, Chennai, India, 2009.
13 R. C. Bansal and M. Goyal, *Activated Carbon Adsorption*, CRC Press, Taylor & Francis Group, Boca Raton, FL, 2005.
14 S. T. S. Kumar, B. S. Kumar, S. Balaji, C. Sanjeeviraja and R. K. Selvan, *Mater. Res. Bull.*, 2011, **46**, 413.
15 (*a*) V. Subramanian, C. Luo, A. M. Stephan, C. Nahm, S. Thomas and B. Wei, *J. Phys. Chem.*, 2007, **111**, 7527; (*b*) M. S. Balathanigaimani, W. G. Shim, M. J. Lee, C. Kim, J. W. Lee and H. Moon, *Electrochem. Commun.*, 2008, **10**, 868; (*c*) T. E. Rufford, D. H. Jurcakova, K. Khosla, Z. H. Zhu and G. Q. Lu, *J. Power Sources*, 2010, **195**, 912.
16 B. L. H. Su, X. G. Zhang, C. H. Mi, B. Gao and Y. Liu, *Phys. Chem. Chem. Phys.*, 2009, **11**, 2195.
17 (*a*) S. Roldan, M. Granda, R. Menendez, R. Santamaría and C. Blanco, *J. Phys. Chem. C*, 2011, **115**, 17606; (*b*) S. Roldan, C. Blanco, M. Granda, R. Menendez and R. Santamaría, *Angew. Chem., Int. Ed.*, 2011, **50**, 1699; (*c*) Q. Li, K. Li, C. Sun and Y. Li, *J. Electroanal. Chem.*, 2007, **611**, 43.
18 (*a*) Y. H. Jun, W. J. Huai, F. L. Qing, L. Y. Zhen, C. S. Hong, C. Yuan, W. J. Li, H. M. Liang, L. J. Ming, L. Zhang and H. Y. Fang, *Sci. Chi. Chem*, 2102, **55**, 1319; (*b*) J. Wu, H. Yu, L. Fan, G. Luo, J. Lin and M. Huang, *J. Mater. Chem.*, 2012, **22**, 19025.
19 (*a*) H. Yu, L. Fan, J. Wu, Y. Lin, M. Huang, J. Lin and Z. Lan, *RSC Adv.*, 2012, **2**, 6736; (*b*) S. Roldan, M. Granda, R. Menendez, R. Santamaria and C. Blanco, *Electrochim. Acta*, 2012, **83**, 241.
20 G. Lota and E. Frackowiak, *Electrochem. Commun.*, 2009, **11**, 87.
21 (*a*) G. Lota, K. Fic and E. Frackowiak, *Electrochem. Commun.*, 2011, **13**, 38; (*b*) S. T. Senthilkumar, R. Kalaiselvan, N. Ponpandian and J. S. Melo, *RSC Adv.*, 2012, **2**, 8937.
22 W. Huang, H. zhang, Y. Huang, W. Wang and S. Wei, *Carbon*, 2011, **49**, 838.
23 W. Xing, C. C. Huang, S. P. Zhuo, X. Yuan, G. Q. Wang, D. H. Jurcakova, Z. F. Yan and G. Q. Lu, *Carbon*, 2009, **47**, 1715.
24 J. Yan, T. Wei, B. Shao, F. Ma, Z. Fan, M. Zhang, C. Zheng, Y. Shang, W. Qian and F. Wei, *Carbon*, 2010, **48**, 1731.
25 S. Roldan, I. Villar, V. Ruiz, C. Blanco, M. Granda, R. Menendez and R. Santamaria, *Energy Fuels*, 2010, **24**, 3422.
26 (*a*) D. Yuan, J. Zheng, N. Kristian, Y. Wang and X. Wang, *Electrochem. Commun.*, 2009, **11**, 313; (*b*) W. Chen, R. B. Rakhi, L. Hu, X. Xie, Y. Cui and H. N. Alshareef, *Nano Lett.*, 2011, **11**, 5165.
27 H. Yu, J. Wu, L. Fu, K. Xu, X. Zhang, Y. Lin and J. Lin, *Electrochim. Acta*, 2011, **56**, 6881.
28 J. Zhou, Y. Yin, A. N. Mansour and X. Zhou, *Electrochem. Solid-State Lett.*, 2011, **14**, A25.
29 K. C. Ng, S. Zhang, C. Peng and G. Z. Chen, *J. Electrochem. Soc.*, 2009, **156**, A846.
30 J. Y. Kim and I. J. Chung, *J. Electrochem. Soc.*, 2002, **149**, A1376.
31 C. P. D. Leon, A. F. Ferrer, J. G. Garcia, D. A. Szanto and F. C. Walsh, *J. Power Sources*, 2006, **160**, 716.
32 Z. Lin, Y. Liu, Y. Yao, O. J. Hildreth, Z. Li, K. Moon and C. P. Wong, *J. Phys. Chem. C*, 2011, **115**, 7120.
33 Y. Chen, X. Zhang, D. Zhang, P. Yu and Y. Ma, *Carbon*, 2011, **49**, 573.
34 W. Wei, X. Cui, W. Chen and D. G. Ivey, *J. Power Sources*, 2009, **186**, 543.
35 G. Sun, K. Li and C. Sun, *Microporous Mesoporous Mater.*, 2010, **128**, 56.
36 (*a*) G. Lota and G. Milczarek, *Electrochem. Commun.*, 2011, **13**, 470; (*b*) H. Yu, J. Wu, L. Fan, K. Xu, X. Zhong, Y. Lin and J. Lin, *Electrochim. Acta*, 2011, **56**, 6881; (*c*) H. Yu, J. Wu, L. Fan, Y. Lin, K. Xu, Z. Tang, C. Cheng, S. Tang, J. Lin, M. Huang and Z. Lan, *J. Power Sources*, 2012, **198**, 402.
37 (*a*) H. A. Andreas, K. Lussier and A. M. Oickle, *J. Power Sources*, 2009, **187**, 275; (*b*) Y. P. Lin and N. L. Wu, *J. Power Sources*, 2011, **196**, 851.